Dynamics of a model colloidal suspension from dilute to freezing

S. D. W. Hannam, P. J. Daivis,* and G. Bryant
School of Science and Centre for Molecular and Nanoscale Physics, RMIT University, GPO Box 2476, Melbourne Vic 3001, Australia
(Received 12 May 2016; published 26 July 2016)

Molecular dynamics simulation was used to study a model colloidal suspension at a range of packing fractions from the dilute limit up to the freezing point. This study builds on previous work by the authors which modeled the colloidal particles with a hard core surrounded by a Weeks-Chandler-Anderson potential with modified interaction parameters, and included an explicit solvent. In this work, we study dynamical properties of the model by first calculating the velocity autocorrelation function, the self-diffusion coefficient, and the mutual diffusion coefficient. We also perform detailed calculations of the colloidal particle intermediate scattering function to study the change in dynamics leading up to the freezing point, and to determine whether the current model can be used to interpret light scattering experiments. We then perform a multiexponential analysis on the intermediate scattering function results and find that the data are fitted well by the sum of two exponentials, which is in line with previous analysis of experimental colloidal suspensions. The amplitudes and decay coefficients of the two modes are determined over a large range of wave vectors at packing fractions leading up to the freezing point. We found that the maximum wave vector at which macroscopic diffusive behavior was observed decreased as the packing fraction increased, and a simple extrapolation shows the maximum wave vector going to zero at the melting point. Lastly, the ratio of the two decay coefficients is compared to the scaling law proposed by Segrè and Pusey [Phys. Rev. Lett. **77**, 771 (1996)]. It was found that the ratio was not constant, but instead was wave vector dependent.

DOI: 10.1103/PhysRevE.94.012619

I. INTRODUCTION

Colloidal systems are ideal for studies of solidification mechanisms. An understanding of crystallization processes in colloidal systems aids in the understanding of phase transitions in other soft matter systems [1,2], with application to materials design [3] and to biology [4]. Crystallization in colloidal suspensions can be studied via light scattering experiments, often using dynamic light scattering (DLS) or x-ray photon correlation spectroscopy (XPCS) [5].

Typical model systems used in light scattering experiments consist of suspensions of spherical particles which are stabilized against aggregation by coating the surface with a short-chained polymer (steric stabilization) or with a charged ionic layer (charge stabilization). The computational model used in this work does not include electrostatic interactions. Therefore, it aims to replicate the dynamics of sterically stabilized suspensions where the interaction is steeply repulsive and is often modeled with hard-sphere interactions. The pioneering work using DLS to study the dynamics of dense colloidal suspensions was done by Pusey, van Megen, and collaborators [6–11].

Computational models are a useful complement to experimental investigations. But, although the computer power available is ever increasing, a full molecular dynamics (MD) treatment of all the interactions present in the system is still computationally unattainable. Because of the complexity of experimental systems, most simulations resort to idealized descriptions, often modeling the systems as single component hard spheres using event driven MD [12] which completely ignores the presence of the solvent. This means the particles in these models move with ballistic dynamics, rather than diffusing through a solvent. These models neglect effects such as the viscoelasticity of the solvent and the momentum transfer that occurs via the solvent [13].

To implicitly take into account the solvent, Brownian dynamics (BD) treats the fluid as a continuum represented by frictional and random forces. This introduces an effective drag on the hard spheres, but usually does not include multibody hydrodynamic interactions (HIs) from the solvent [14,15]. Incorporating two-body HIs in BD in a simplified way requires the use of hydrodynamic tensors such as the Yamakawa-Rotne-Prager (YRP) tensors [16–18]. However, BD-YRP hydrodynamics is only valid for relatively dilute suspensions and can be quite computationally expensive. Alternative techniques that have been developed to include HIs include lattice-Boltzmann [19,20], dissipative particle dynamics [21], and stochastic rotation dynamics [22,23], all of which involve coarse graining the solvent.

Few attempts have been made to include solvent explicitly into the simulation by calculating the equations of motion for both the colloidal particles and the solvent directly. This is simply because in order to match the size and mass ratio of experimental colloidal suspensions, the simulation would require in the order of tens of millions of solvent molecules for every colloidal particle. This is clearly beyond the reach of current computational capabilities, so smaller size and mass ratios have to be used. Vrabecz and Toth [24] studied the effect of explicitly adding a second smaller HS particle ($\frac{1}{5}$th and $\frac{1}{10}$th the diameter of the larger particle) on the structural properties of the fluid. They found that including the second smaller species caused a change in the radial distribution function of the larger particles in the fluid. This was evident through sharpening in the main peak, showing that the presence of the smaller particles causes a very strong depletion attraction between the larger particles.

Previous work done by the authors expanded on the explicit solvent model by including a second species with a smaller

*peter.daivis@rmit.edu.au

mass ($\frac{1}{50}$th the mass of the larger particles) and smaller size ($\frac{1}{4}$th the diameter) to represent the solvent [25]. In this model, the colloidal particles were modeled using a Weeks-Chandler-Anderson (WCA) potential which was modified to include a hard core, while the solvent was modeled using a simple WCA potential. In agreement with previous work, it was found that introduction of the second smaller species caused strong depletion attractions between the larger species [24]. These strong depletion forces are not present in experimental HS colloidal suspensions, and are purely due to the relatively small size ratio that had to be employed in the simulations due to computational limitations. Because the diameter of the two particles is of the same order, there is an excluded volume around the colloidal particles that gives rise to significant depletion effects.

Since the depletion effects were caused by the large excluded volume, it could be effectively eliminated by reducing the hard-core parameter in the colloidal-solvent pair interaction [25]. This allowed the solvent to effectively penetrate the colloid, which can be seen as unphysical, but the model was found to replicate the properties of an experimental colloidal suspension. The static structure factor, phase behavior, and crystal structure were all found to agree with experimental results. With the apparent success of this model in replicating the behavior of real colloidal suspensions for these few key features, it remains to be seen how well it matches the dynamical behavior as represented by other properties (such as diffusion coefficients and the intermediate scattering function) and whether the model can be used as a complement to light scattering experiments.

Therefore, one of the aims of this work is to expand on the previous work by calculating a number of key transport coefficients over a wide range of colloid packing fractions (also referred to as volume fractions) from the dilute fluid up to the freezing point. Then, we compare the calculations of the model with available experimental results to determine the level of agreement. The other goal of this paper is to use this model to obtain accurate calculations for the intermediate scattering function at packing fractions approaching the freezing point.

In the liquid state, the empirical fit to the intermediate scattering function usually takes the form of a single or double exponential [26,27]. In extremely dilute systems at low wave vector, DLS yields a single exponential decay with a wave vector independent diffusion coefficient. This is in line with what was found in previous work using this model [25]. As the packing fraction increases, the diffusion coefficient becomes wave vector dependent, but the decay is still well approximated by a single exponential.

At moderate packing fractions, a second decay mode is observed and the data are fitted with two exponentials with different effective diffusion coefficients [9,27]. These two empirical modes are often associated with short-time and long-time diffusion coefficients, where the former is associated with movement of the colloidal particles in its local cage while the latter is associated with diffusion over larger length scales [9]. This interpretation of the two modes has not been verified, and an exact relationship between the decay coefficients and transport or thermodynamic properties has not been made. Even so, Segrè and Pusey [28] proposed an empirical scaling law where the ratio of the two effective diffusion coefficients is approximately constant for highly concentrated colloidal suspensions over a broad range of wave vectors around the structure factor peak.

The validity of this scaling law has been called into question, with Lurio *et al.* [29] failing to observe the scaling in XPCS experiments on a charge-stabilized colloidal suspension. This was thought to be either because the colloids were charge stabilized (rather than sterically stabilized) or because XPCS gives different results to DLS. Martinez *et al.* [5] showed that the results of XPCS and DLS experiments are consistent, ruling out the latter explanation. They were able to see the scaling behavior over several decades in time but not in the long-time limit. More recent work by Orsi *et al.* [27] studied a system very similar to that used by Martinez and Segrè, and found that the scaling law did hold for high concentration sterically stabilized colloids.

A systematic study of the individual decay modes over a large range of packing fractions and wave vectors is difficult to do experimentally. In particular, it is difficult to access low wave vectors using existing techniques. Therefore, we choose to use MD to calculate the intermediate scattering function and use a multiexponential analysis to decompose its individual contributions in order to complement the experimental investigation.

The outline of this paper is as follows: First, we give a summary of the computational model used, and describe how we calculated the self- and mutual diffusion coefficients in equilibrium MD using time correlation functions. Then, we systematically study the behavior of the correlation functions and the self- and mutual diffusion coefficient from an extremely dilute state up to packing fractions just below the freezing point in order to observe any major changes that occur in the approach to freezing. Finally, a multiexponential analysis is carried out on the colloidal particle intermediate scattering function from small wave vectors to just past the structure factor peak. This is done for higher packing fractions approaching the freezing point. We discuss the individual decay modes that are observed and their wave vector and packing fraction dependence. We then test the scaling relationship proposed by Segrè and Pusey [28] to see if we also find a constant ratio of the short- and long-time diffusion coefficients.

II. THEORY

A. Thermodynamic and transport coefficients

Transport coefficients can be determined by calculating time correlation functions (TCFs) and using Green-Kubo relations [30]. In general, the time correlation function of a Fourier component of the microscopic property A takes the form

$$C(k,\tau) = \langle A(\mathbf{k},\tau)A^*(\mathbf{k},0)\rangle, \tag{1}$$

where $A(\mathbf{k},\tau)$ is now the spatial Fourier transform of the microscopic variable $A(\mathbf{r},\tau)$ and * indicates the complex conjugate. The angular brackets represent an ensemble average and τ represents the delay time in the correlation function. The wave vector $\mathbf{k}$ being studied in MD simulations must be consistent with the periodic boundary conditions of the

simulation box:

$$\mathbf{k} = \frac{2\pi}{L}(n_1,n_2,n_3), \tag{2}$$

where n_i is an integer and L is the length of the simulation box (in this work the box is cubic so $L_x = L_y = L_z$). The correlation function $C(k,\tau)$ only depends on the magnitude $k = |\mathbf{k}|$ as the average is done over all $\mathbf{k}$ of equal magnitude (as the fluid is isotropic). Also, from Eq. (2) we see that the lowest k value that can be measured in an MD simulation is $k = 2\pi/L$.

In this work, we study correlation functions of particular microscopic variables that give useful information on properties of the colloidal suspension. The self-diffusion coefficient of the colloidal particles D_s can be calculated from the integral of the velocity autocorrelation function $C(\tau)$ by [31]

$$D_s = \int_0^\infty C(\tau)d\tau = \frac{1}{3}\int_0^\infty \langle \mathbf{v}_i(\tau)\cdot\mathbf{v}_i(0)\rangle d\tau, \tag{3}$$

where $\mathbf{v}_i$ is the velocity of colloidal particle i and the average is done over all colloidal particles. Self-diffusion is related to the diffusion of a particle in the absence of temperature and/or concentration gradients. But, in the presence of such gradients other transport coefficients are defined. The linearized macroscopic diffusion equation for species 1 (which represents the colloidal particles) in a binary fluid is [32]

$$\frac{\partial c_1}{\partial t} = D_m\nabla^2 c_1 + D'\nabla^2 T, \tag{4}$$

where c_i refers to the mass fraction of species i, D_m is the mutual diffusion coefficient, D' is the thermal-diffusion coefficient, and T is the temperature. The coefficients D_m and D' can be calculated from nonequilibrium MD simulation by setting up a system with a concentration/temperature gradient. They can also be calculated from equilibrium MD by relating them to the phenomenological coefficients $L_{\alpha\beta}$ which can be calculated from TCFs using Green-Kubo relations. As we will see later, the mutual diffusion coefficient D_m governs the decay of the intermediate scattering functions in the low wave vector limit.

A well known expression for the mutual diffusion coefficient D_m is given by [32]

$$D_m = \frac{L_{11}}{\rho c_2 T}\left(\frac{\partial\mu_1}{\partial c_1}\right)_{p,T}, \tag{5}$$

where ρ is the total mass density of the fluid and μ_1 is the chemical potential per unit mass of the colloidal particles. L_{11} is the phenomenological coefficient given in the Green-Kubo relations as

$$L_{11} = \lim_{\tau\to\infty}\int_0^\tau A_{11}(\tau)d\tau \tag{6}$$

and

$$A_{11}(\tau) = \frac{V}{3k_BT}\langle \mathbf{J}_1(\tau)\cdot\mathbf{J}_1(0)\rangle, \tag{7}$$

where k_B is Boltzmann's constant and V the volume of the system. The microscopic expression for the diffusive mass flux $\mathbf{J}_1$ of the colloidal particles takes the form

$$\mathbf{J}_1 = \frac{1}{V}\sum_{i=1}^{N_1} m_1(\mathbf{v}_i - \mathbf{v}), \tag{8}$$

where m_1 is the mass of a colloidal particle and $\mathbf{v}$ is the average streaming velocity ($\mathbf{v} = 0$ for an equilibrium fluid).

Apart from the usual transport coefficients, we also calculated the intermediate scattering function $F_{\alpha\beta}(k,\tau)$ which is also measured in light scattering experiments. This can be done in equilibrium MD simulation by calculating the correlation function of the Fourier transform of the number density:

$$n_\alpha(\mathbf{k},t) = \frac{1}{\sqrt{N}}\sum_{i=1}^{N_\alpha}\exp[-i\mathbf{k}\cdot\mathbf{r}_i(t)], \tag{9}$$

where N is the total number of particles, N_α is the number of particles of species α, and $F_{\alpha\beta}(k,\tau)$ is given as

$$F_{\alpha\beta}(k,\tau) = \frac{\langle n_\alpha(\mathbf{k},\tau)n^*_\beta(\mathbf{k},0)\rangle}{S_{\alpha\beta}(k)}, \tag{10}$$

where the static structure factor $S_{\alpha\beta}(k)$ is defined as

$$S_{\alpha\beta}(k) = \langle n_\alpha(\mathbf{k},0)n^*_\beta(\mathbf{k},0)\rangle. \tag{11}$$

From the calculations of the $F_{\alpha\beta}(k,\tau)$ we are able to make comparisons with experimental data.

The decay of $F_{11}(k,\tau)$ can be related to the mutual diffusion coefficient D_m in the macroscopic diffusive limit. From the thermodynamic point of view, D_m relates the diffusive mass flux to the gradient in the concentration. From the microscopic point of view, such gradients arise in an equilibrium suspension from local fluctuations, and the decay of these fluctuations is governed by the same equation as the decay of macroscopic gradients.

Therefore, starting with the balance equation for the mass fraction of species 1 we can Fourier transform Eq. (4) into k space which gives

$$\frac{\partial c_1(k,t)}{\partial t} = -D_m k^2 c_1(k,t), \tag{12}$$

where we have neglected thermal diffusion as this effect is small in comparison to mutual diffusion. After multiplying both sides of Eq. (12) by the complex conjugate of the initial time value $c_1^*(k,0)$ and ensemble averaging, the solution becomes

$$F_{11}(k,\tau) = \frac{\langle c_1(k,\tau)c_1^*(k,0)\rangle}{\langle |c_1(k,0)|^2\rangle} = \exp(-k^2D_m\tau), \tag{13}$$

which corresponds to the intermediate scattering function of the colloidal particles. This macroscopic relationship is only expected to hold in the macroscopic diffusive limit. Therefore, the mutual diffusion coefficient governs the decay of the intermediate scattering function in the $k \to 0$ limit.

B. Calculation of the thermodynamic factor

In order to calculate the mutual diffusion coefficient D_m [defined in Eq. (5)], accurate values are needed for both the thermodynamic factor $\partial\mu_1/\partial c_1$ and phenomenological coefficient L_{11}. L_{11} can be calculated from Green-Kubo theory, but $\partial\mu_1/\partial c_1$ is more difficult to calculate. One of the best

ways to calculate it is using the theory presented by Kirkwood and Buff (KB) which relates the thermodynamic factor to the integral of the radial distribution functions $G_{\alpha\beta}$ [33]. A conversion of the original KB relations to the mass fraction units was done by Zhou and Miller [34] and is given for a binary fluid as

$$\left(\frac{\partial \mu_1}{\partial c_1}\right)_{p,T} = \frac{V^2}{\rho \langle |c|^2 \rangle}, \tag{14}$$

where

$$\langle |c|^2 \rangle = \frac{m_1^2 m_2^2 x_1 x_2 n^2 N}{\rho^4}[1 + x_1 x_2 n(G_{11} + G_{22} - 2G_{12})]. \tag{15}$$

Here, m_α and x_α are the mass and number fraction of species α, respectively, and n is the total number density of the fluid. The volume integrals of the radial distribution functions $G_{\alpha\beta}$ are calculated from

$$G_{\alpha\beta} = \int [g_{\alpha\beta}(\boldsymbol{r}) - 1]\, d\mathbf{r} = 4\pi \int r^2 [g_{\alpha\beta}(r) - 1] dr, \tag{16}$$

where $g_{\alpha\beta}(r)$ is the radial distribution function of species α and β. These integrals can be difficult to calculate as statistical error in $g_{\alpha\beta}$ at large r is magnified by the factor of r^2, so the numerical integrals may not converge. Therefore, calculation of $G_{\alpha\beta}$ usually requires very accurate data for $g_{\alpha\beta}(r)$ and fitting a function to the tail to evaluate the integral [35,36].

Instead of calculating this integral, it can be simpler to calculate the values of $G_{\alpha\beta}$ through the static structure factors $S_{\alpha\beta}(k)$. It is well known that the partial structure factors are related to the Fourier transforms of the radial distribution functions through [31]

$$S_{\alpha\beta}(k) = x_\alpha \delta_{\alpha\beta} + x_\alpha x_\beta n \int g_{\alpha\beta}(r) \exp(i\mathbf{k} \cdot \mathbf{r}) d\mathbf{r}. \tag{17}$$

Assuming that the fluid is isotropic and writing the constant part of the radial distribution explicitly, this can be rewritten as

$$S_{\alpha\beta}(k) = x_a \delta_{\alpha\beta} + 4\pi x_\alpha x_\beta n \int r^2 [g_{\alpha\beta}(r) - 1] \exp(i\mathbf{k} \cdot \mathbf{r}) dr + (2\pi)^3 x_\alpha x_\beta n \delta(k). \tag{18}$$

Comparing this with the expression given for $G_{\alpha\beta}$ in Eq. (16) we see that, if we ignore the contribution of the delta function at zero wave vector, we can write

$$G_{\alpha\beta} = 4\pi \int r^2 [g_{\alpha\beta}(r) - 1] dr = \lim_{k \to 0} 4\pi \int r^2 [g_{\alpha\beta}(r) - 1] \exp(i\mathbf{k} \cdot \mathbf{r}) dr, \tag{19}$$

therefore,

$$G_{\alpha\beta} = \frac{1}{x_\alpha x_\beta n}\left[\lim_{k \to 0} S_{\alpha\beta}(k) - x_\alpha \delta_{\alpha\beta}\right]. \tag{20}$$

So, by calculating the low-k values of the partial structure factors $S_{\alpha\beta}(k)$, and extrapolating $k \to 0$, the values of $G_{\alpha\beta}$ can be calculated in a much simpler way. This method offers a much easier method of calculation $G_{\alpha\beta}$ than through the integral given in Eq. (16) directly. An alternate derivation of a relationship between the thermodynamic factors and the $S_{\alpha\beta}(k \to 0)$ values was previously done by Nichols and coworkers [37], although their definition of the thermodynamic factor differs.

C. Multiexponential analysis

As stated earlier, the intermediate scattering function is defined as the autocorrelation function of a Fourier component of the number density. Barocchi and coauthors [38–40] showed that the complete behavior of any normalized autocorrelation function of a classical many-body system can be described by a generalized Langevin equation, the exact solution of which can be written as an infinite sum of exponential functions

$$C(t) = \sum_{j=1}^{\infty} A_j \exp(z_j t), \tag{21}$$

where A_j and z_j are mode amplitudes and decay coefficients, respectively. Such modes can be associated with relaxation channels in the system. If A_j and z_j are complex quantities, the corresponding mode and its complex conjugate are both present in the series and, taken together, they represent an exponentially damped oscillation. Otherwise, real A_j and z_j define a purely exponential decay.

An approximate solution to the generalized Langevin equation can be found by truncating Eq. (21) at a finite number of terms. The behavior of the coefficients can then be studied by fitting the resulting function to experimental and simulation data. This procedure can be difficult, due to the large number of free fitting parameters.

Barocchi and coauthors found that the number of free fitting parameters can be reduced by constraining the solution. They showed that the zero time properties of the solution given in Eq. (21) must obey the relation

$$\left[\frac{d^m C(t)}{dt^m}\right]_{t=0} = 0, \tag{22}$$

where m is an odd integer. When a finite number of exponential terms are retained, Eqs. (21) and (22) can only be valid for m up to a certain value depending on the approximation level and the model assumed. The combination of Eqs. (21) and (22) allows the number of free fitting parameters to be reduced.

As we shall show later in this work, the decay of the intermediate scattering function $F(k,\tau)$ at a particular wave vector can be accurately described by the superposition of two real exponentials (for the two diffusive decay modes) and one complex conjugate pair exponential (for the short-time nondiffusive behavior). Therefore, in this work we will approximate the solution by retaining the first three terms in Eq. (21); this results in

$$F(k,t) \approx A_1 \exp(z_1 t) + A_2 \exp(z_2 t) + (A_3' \pm i A_3'') \exp[(z_3' \pm i z_3'')t]. \tag{23}$$

In line with usual experimental analysis, we can refer to the first two decay modes as the short-time and long-time diffusion modes with effective short-time D_s and long-time D_L diffusion coefficients. The complex exponential can also be simplified

into a damped cosine form. Doing this results in

$$F(k,t) \approx A_s \exp(-k^2 D_s t) + A_L \exp(-k^2 D_L t) + A_d \exp(\alpha t)\cos(-\beta t + \phi), \quad (24)$$

where all coefficients are wave vector dependent and we have included a factor of k^2 in the real exponentials. Equation (24) is the final form that is fitted to the simulation data.

Fitting Eq. (24) to simulation data requires optimization of eight free fitting parameters. But, this number can be reduced by constraining the solution using the relationship given in Eq. (22) for $m = 1$ and 3. Also, the normalization condition of $F(k,t = 0) = 1$ allows an additional variable to be eliminated, resulting in the total elimination of three free parameters, thus reducing the computational complexity of the problem.

The fitting of the multiexponential model was performed by means of a program run in the MATLAB [41] environment, carried out by a built-in nonlinear least squares algorithm. The implementation of the three constraints was done by using the inbuilt solve function to give expressions for the chosen dependent parameters in terms of the independent ones.

III. SIMULATION METHODS

The pair potential and parameters for our simulations are identical to previous work [25] but we will include a brief explanation here. We modeled the colloidal particle and solvent using a Weeks-Chandler-Andersen (WCA) potential (a shifted and truncated Lennard-Jones potential) which is modified to include a hard core. The potential takes the form

$$\phi(r_{ij}) = \begin{cases} \infty & \text{if } r_{ij} \leqslant c_{ab}, \\ 4\epsilon\left[\left(\frac{\sigma}{r_{ij}-c_{ab}}\right)^{12} - \left(\frac{\sigma}{r_{ij}-c_{ab}}\right)^{6}\right] + \epsilon & \text{if } c_{ab} < r_{ij} < c_{ab} + 2^{1/6}, \\ 0 & \text{otherwise,} \end{cases}$$

where r_{ij} is the center-to-center distance between the particles i and j, ϵ is the depth of the potential well, σ is the nominal length scale of the potential (in this work $\epsilon = \sigma = 1$ and therefore all results are given in reduced units). The c_{ab} parameter introduces a hard core to the potential where a and b denote the two interacting species. This creates an excluded region which is used to increase the size of the colloidal particle relative to the solvent. A diagram of the potential is shown in Fig. 1.

In this work, we keep the values of the c_{ab} fixed for the colloid-colloid (c_{11}) and solvent-solvent (c_{22}) interactions at 3.03 and 0.000, respectively. The c_{12} parameter for the colloid-solvent interaction is also set to 0.000 to remove the depletion effects that are inherent in systems with different sized particles. In usual hard-sphere simulations the diameter of the particle is clear, but in this work we are using a hard core plus a WCA repulsive potential. This WCA repulsive potential adds an extra diameter that is not clearly defined.

Previous work has been done by Hess *et al.* to determine expressions for the effective diameter of WCA particles as a function of temperature [42]. These authors found that the method which gave the best agreement with the MD results was to define the effective diameter d to be when the interaction potential is equal to Boltzmann's constant times the temperature $\phi(d) = k_B T$. At the reduced temperature of 1.0 used in this work, this gives an extra diameter of σ to the particles due to the WCA repulsion. This gives the colloidal particles an effective diameter of 4.03 times the diameter of the solvent particles.

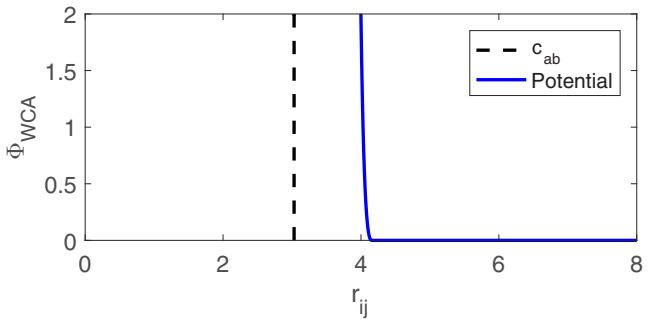

FIG. 1. Diagram of pair potential between colloidal particles with $\epsilon = \sigma = 1.00$ and $c_{ab} = 3.03$.

The mass of the colloidal particle was set with the goal of making it approximately neutrally buoyant in the solvent. The mass needed to do this was calculated in the same way as McPhie [43], which for a size ratio d_1/d_2 of 4.03 gave a mass ratio m_1/m_2 of 50. Therefore, we used a mass of 1.0 for the solvent particles and a mass of 50.0 for the larger particles. This size and mass ratio has been shown to be large enough for the larger particle to behave as a Brownian particle in the solvent [44].

All simulations were run using the MD package LAMMPS [45] and the results were post-processed using in-house code. Simulations at each packing fraction were done under NPT conditions at a reduced temperature of 1.00 and reduced pressure of 7.85. The time integration scheme used follows the time-reversible measure-preserving Verlet integrator derived by Tuckerman *et al.* [46] with a time step of 0.005. The temperature is held fixed using a Nose-Hoover thermostat while the pressure is held fixed using a Nose-Hoover type barostat, both used a damping parameter of 10. This was done in order to better replicate the experimental conditions of a real colloidal suspension. All simulations were done with a total of 108 000 particles, except for one larger system which was done in order to calculate data for small-k values of the intermediate scattering function at the packing fraction of 0.49. This simulation had 864 000 particles. Table I gives the exact number of particles used in the simulations, along with the average volume and calculated packing fraction. The packing fraction Φ was calculated from

$$\Phi = \frac{\pi N_c d^3}{6V}, \quad (25)$$

TABLE I. Number of solvent particles N_s, colloidal particles N_c, average volume $\langle V \rangle$, and packing fraction Φ for the systems studied.

System No.	N_s	N_c	$\langle V \rangle$	Φ
1	107,967	33	128,606	0.01
2	107,652	348	128,550	0.09
3	107,325	675	128,597	0.18
4	106,988	1012	128,600	0.27
5	106,650	1350	128,887	0.36
6	106,313	1687	129,085	0.44
7	106,145	1855	129,315	0.49
8	849,160	14,840	1,028,848	0.49

where d is the diameter of the colloidal particles ($d = 4.03$ for all colloidal particles). In our previous work, we showed that calculating Φ for this system based on Eq. (25) resulted in a phase behavior that matched closely to that of a single component HS system [25].

In the following sections, we will be mostly calculating properties of the larger particles (meant to represent the colloidal particles). Because of this, subscripts designating species will be dropped and unless otherwise stated the properties being measured are for the colloidal particles only (i.e., the colloidal particle intermediate scattering function $F_{11}(k,\tau)$ will just be represented as $F(k,\tau)$, etc).

IV. RESULTS

A. Velocity autocorrelation function and self-diffusion coefficient

Figure 2 displays results for the absolute value of the colloidal particle velocity autocorrelation function $|C(\tau)|$. It is displayed on a log-log scale as the decay of $C(\tau)$ covers multiple orders of magnitude across a number of decades in time. The curves shown cover a large range of packing fractions from a dilute system ($\Phi = 0.09$) to a system at a packing fractions slightly lower than the freezing point ($\Phi = 0.49$). C(τ) has been calculated previously for this model [25], but we include it here again as the quality of the data has been greatly improved which allows a more thorough comparison with pure HS simulation results, as well as experimental data.

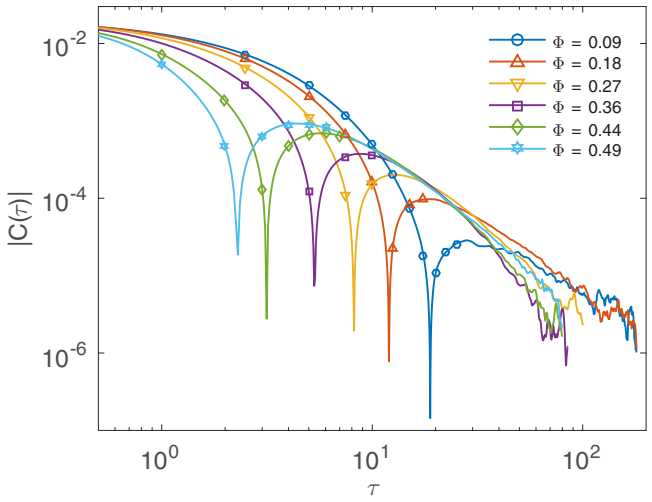

FIG. 2. Plot of the colloidal particle velocity autocorrelation function C(τ) at packing fractions leading up to the freezing point. The points where $C(\tau)$ cross zero may be seen as a sharp spike downward in this log-log graph.

The most thorough study to date on the velocity autocorrelation function for a pure HS system (no solvent) was done by Williams and co-workers [47,48]. They were able to observe the $-\frac{3}{2}$ power-law long-time tail (which is the manifestation of diffusing transverse modes) and velocity reversals (which are the result of damped compression modes [49]). For stable fluids, velocity reversals were only observed for high packing fractions ($\Phi \geqslant 0.44$). In Fig. 2, we also observe velocity reversals {indicated by the spike downward on the log[$|C(\tau)|$] plot where $C(\tau)$ becomes negative}. The reversals are seen for all Φ shown ($0.09 \leqslant \Phi \leqslant 0.49$), with the time it takes for the reversals to occur decreasing as Φ increases.

Both the pure HS (without solvent) and our model (with solvent) can be compared with available experimental data. It is very difficult to determine experimentally the complete behavior of C(τ). The initial decay of C(τ) (which gives the initial crossing through zero) is difficult to obtain accurately. Even so, reversals in $C(\tau)$ are observed at packing fractions as low as $\Phi = 0.289$ in experimental colloidal suspensions [50] where the long-time decay of $C(\tau)$ occurs from below zero. This is consistent with the results from our model, but disagrees with the results from the pure HS system. The mismatch between the sign of $C(\tau)$ at low to moderate Φ for the single component HS fluid was pointed out in our previous work [25], indicating that the current model possesses dynamics which better resemble that of an experimental colloidal suspension. A possible reason why the pure HS model fails to predict the reversals at low to moderate packing fractions is because it neglects the solvent, and therefore ignores hydrodynamic effects and momentum transfer via the solvent, both of which could cause velocity reversals.

However, current data for this model suffer from the same limitations as experiment, in that the power-law long-time decay of C(τ) falls within the noise and cannot be observed. This is due to the smaller number of colloidal particles and the much larger mass, which results in smaller velocities.

The colloidal particle self-diffusion coefficient D_s is related to the ability of an individual colloidal particle to diffuse through the liquid. This property was calculated from Eq. (3) and is shown in Fig. 3. We have normalized the data by dividing by the dilute limit value of $(5.93 \pm 0.05) \times 10^{-2}$. The maximum value of D_s occurs in the dilute limit as the motion is not hindered by direct interactions with other colloidal particles.

As the packing fraction increases, the ability of a single colloidal particle to diffuse through the fluid is hindered. This results in a decrease of the self-diffusion coefficient. In Fig. 3 it can be seen that results from previous Brownian dynamics simulations by Moriguchi [51] overpredict D_s when compared to experimental systems [52,53]. Banchio *et al.* [54] were able to show that an inclusion of a hydrodynamic correction brought BD and experiment into agreement.

The current model also overestimates D_s (as seen in Fig. 3) even though the solvent (and therefore hydrodynamic) effects are included. This disagreement could be due to the modified

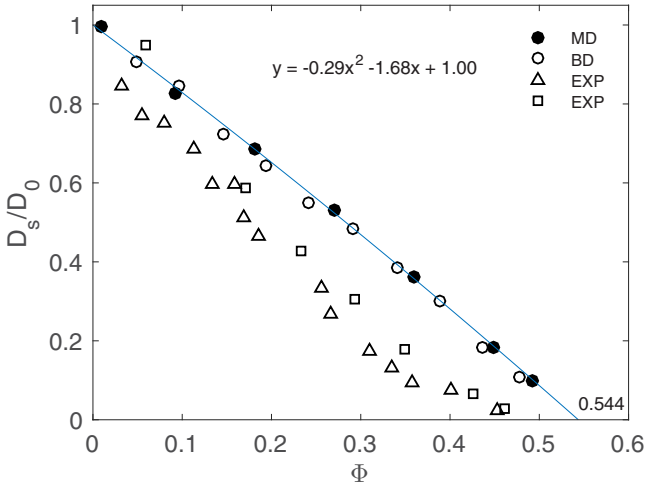

FIG. 3. Plot of the normalized colloidal particle self-diffusion coefficient D_s/D_0 against packing fraction. Filled circles: our MD data; open circles: BD data of Moriguchi [51]; triangles: experimental data of van Megen and Underwood [52]; squares: experimental data of van Blaaderen *et al.* [53]. Quadratic line of best fit to MD data with the numerical value of x intercept (at 0.544) also shown.

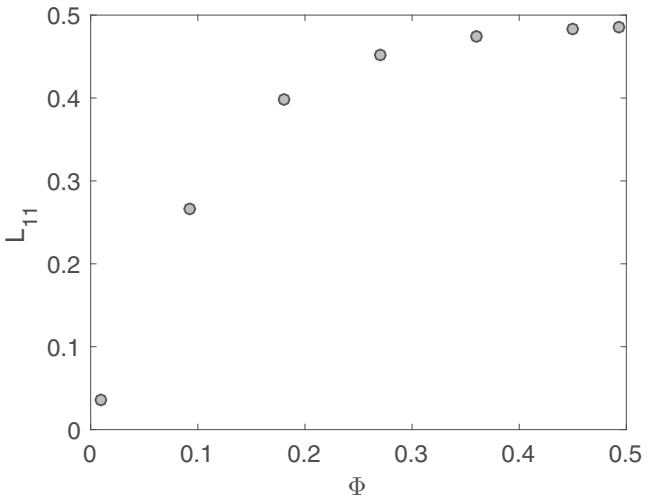

FIG. 4. Plot of the phenomenological coefficient L_{11} calculated from the integral of the colloidal particle mass flux autocorrelation function.

interaction parameters used to reduce the depletion effects ($c_{12} = 0$). By reducing the c_{12} parameter, the volume of the colloid as seen by the solvent is much lower than the volume used in the calculation of the packing fraction. This may have the effect of diluting the hydrodynamic interactions.

To see where D_s extrapolates to zero (where the free movement of the colloidal particles is completely removed), a quadratic function was fitted to the data and the x intercept was calculated. This is found to occur at $\phi = 0.544 \pm 0.010$ which is within the uncertainty of the melting point $\phi = 0.545$ where the hard spheres fully crystallize. This indicates that the diffusive motion of the colloids is frozen out at this point.

The self-diffusion coefficient of real colloidal suspensions can be measured in DLS via the self-intermediate scattering function [55]. From the self-intermediate scattering function the mean squared displacement can be determined, which is related to the so called short- and long-time self-diffusion coefficients. Interestingly, the normalized self-diffusion coefficient of an experimental glass forming system has been shown to go to zero at its glass transition [55], rather than the melting point.

B. Mutual diffusion coefficient

In this model (as in real colloidal suspensions) the solvent is explicitly present and so we have a binary fluid with a single mutual diffusion coefficient [32]. Calculation of D_m [definition given in Eq. (5)] requires accurate values of the phenomenological coefficient L_{11} and the thermodynamic factor $\partial\mu_1/\partial c_1$. We will outline here how these two quantities were calculated.

The phenomenological coefficient L_{11} was calculated from the mass flux correlation function of the colloidal particles defined in Eqs. (6), (7), and (8). The mass flux correlation function was calculated every 5 time steps out to a maximum delay time of 25 000 time steps. Numerical integration with the trapezoid rule was performed on the correlation function and the integrals were found to converge. The values of the integral for each packing fraction are shown in Fig. 4. L_{11} is shown to increase as Φ increases, but the rate of increase (given by the slope of the plot) decreases as the freezing point is approached. At the freezing point, the slope is observed to almost go to zero, and L_{11} appears to plateau.

The second quantity that needs to be calculated is the thermodynamic factor $\partial\mu_1/\partial c_1$ which is related to the integrals of the radial distribution functions $G_{\alpha\beta}$. There are a number of different methods available to calculate the thermodynamic factors from MD simulation, such as through the numerical integration of the radial distribution functions [35], the Widom test particle insertion method [56], from density fluctuations of a smaller subsystem embedded in simulation box [57], or through the static structure factors [37]. In this work, we obtained the thermodynamic factor through the static structure factors by using Eq. (20). It is important to note that Eq. (20) differs from the expression given by Nichols and Wheeler [58] who previously proposed a similar method. This is because the definition of the thermodynamic factors is different, but both methods produce the same value for D_m when combined with their complete expression.

As an example of how the $S_{\alpha\beta}(k \to 0)$ values were calculated for each packing fraction, Fig. 5 shows a plot of the static structure factors S_{11} (colloid-colloid), S_{12} (colloid-solvent), and S_{22} (solvent-solvent) of the system at a packing fraction of 0.49. The data were plotted against k^2 as the $S(k)$ should be an even function of k, and fifth order polynomials in k^2 were fitted to the low-k data. Although it is possible that $S(k)$ could be a nonanalytic function of k, and could therefore also depend on odd or fractional powers of $|k|$, we saw no evidence of this in our data. By extrapolating the polynomial in k^2 back to zero k we were able to accurately determine $S_{\alpha\beta}(k \to 0)$ values.

This was done for a range of packing fractions from an extremely dilute fluid ($\Phi = 0.01$) up to a high density fluid ($\Phi = 0.49$). The highest density fluid is slightly below the freezing point that occurs at $\Phi_F = 0.494$. The values of $S_{\alpha\beta}$

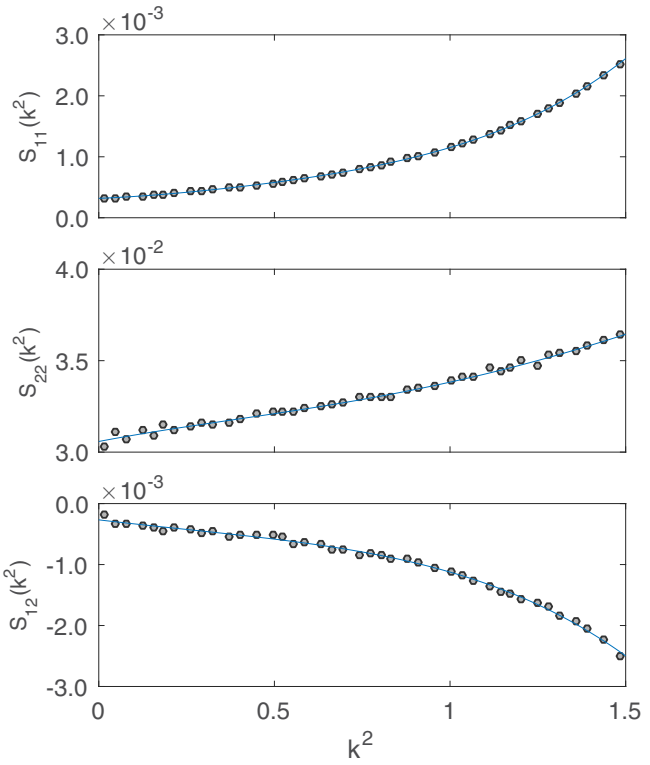

FIG. 5. Plot of the low-k behavior of the static structure factors: S_{11} (colloid-colloid), S_{12} (colloid-solvent), and S_{22} (solvent-solvent) of a system at a packing fraction of 0.49. A fifth order polynomial line of best fit was used to obtain $S_{\alpha\beta}(k \to 0)$ values.

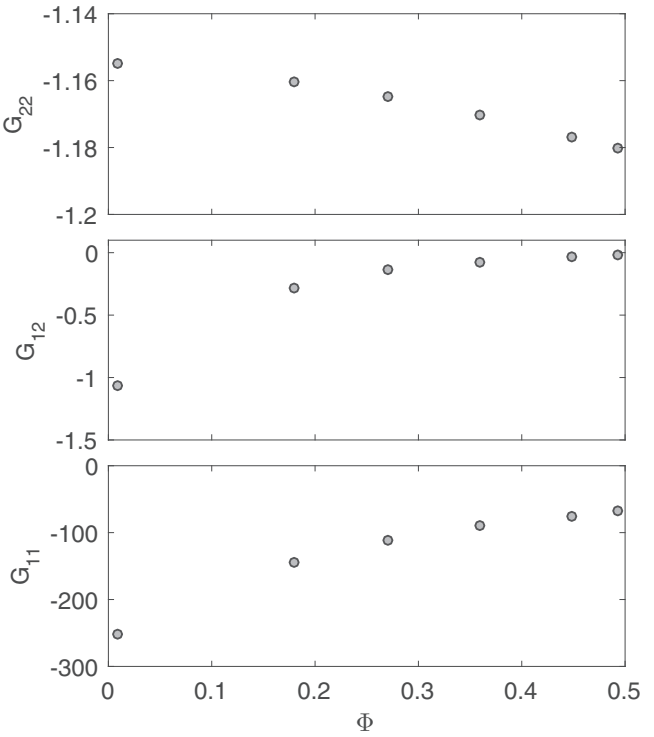

FIG. 6. Plot of the radial distribution function integrals of G_{11} (colloid-colloid), G_{12} (colloid-solvent), and G_{22} (solvent-solvent) at packing fractions Φ leading up to the freezing point.

calculated for each packing fraction were used in (20) to calculate $G_{\alpha\beta}$, which are shown in Fig. 6. The quantities G_{12} and G_{22} have almost negligible contribution to the calculation of the thermodynamic factor $\partial\mu/\partial c_1$ as they are two orders of magnitude smaller than G_{11}. The magnitude of G_{11} decreases as Φ increases, and this results in an increase in $\partial\mu/\partial c_1$ as the two are inversely related [from Eqs. (14) and (15)]. The values of $G_{\alpha,\beta}$ were used in Eqs. (14) and (15) to calculate $\partial\mu/\partial c_1$ for each Φ; these are plotted in Fig. 7. The thermodynamic factor shows a decrease at low concentration, but increases greatly on the approach to the freezing point.

Using the values given for L_{11} and $\partial\mu_1/\partial c_1$, the mutual diffusion coefficient D_m was calculated and is shown in Fig. 8. The mutual diffusion coefficient D_m shows an increase on the approach to the freezing point. From the contributions of L_{11} and $\partial\mu/\partial c_1$ in Figs. 4 and 7 we see that this increase in D_m results mainly from the $\partial\mu/\partial c_1$ contribution rather than from L_{11}, as the latter quantity approaches a plateau near the freezing point.

Equation (13) predicts that the low-k values of the intermediate scattering function will decay faster at higher packing fractions, even as the ability of the individual colloidal particles to diffuse through the liquid decreases on the approach to the freezing point. This results in a broadening of the decay times between the small wave vector and large wave vector decay, which will be shown later.

C. Intermediate scattering function

In this section, calculations of the colloidal particle intermediate scattering function $F(k,\tau)$ will be shown for the higher packing fractions Φ leading up to the freezing point. The systems studied are described in Table I. The wave vectors studied were those consistent with the periodic boundaries of the simulation box [given in Eq. (2)] up to $n_1 = n_2 = n_3 = 15$. In this section, we will report wave vectors in the dimensionless

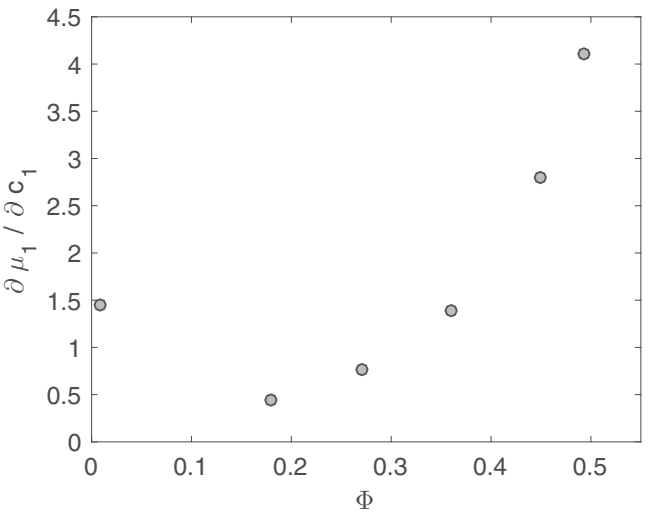

FIG. 7. Plot of the thermodynamic factor $\partial\mu/\partial c_1$ at packing fractions Φ leading up to the freezing point.

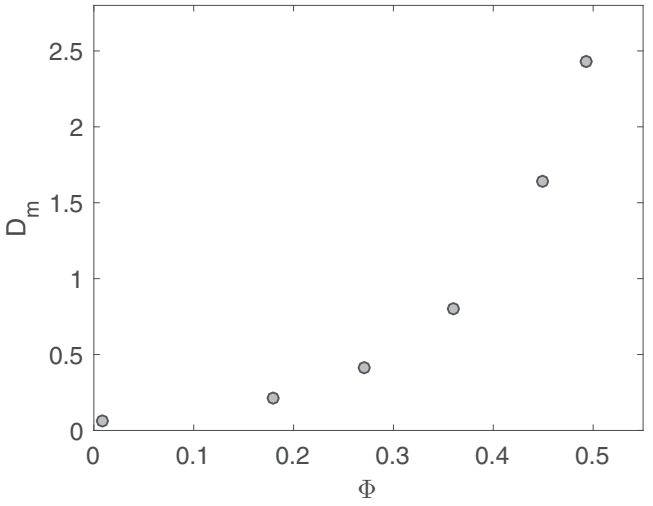

FIG. 8. Plot of the mutual diffusion coefficient D_m at packing fractions Φ leading up to the freezing point.

form kd where d is the diameter of the colloidal particles. This allows direct comparison with corresponding kd values measured in light scattering experiments.

To show the change in behavior of $F(k,\tau)$ leading up to the freezing point, we have displayed the calculations of $F(k,\tau)$ at the packing fractions of 0.27, 0.36, and 0.49 in Fig. 9 (data given as symbols). The wave vectors shown have been chosen to cover a range from the lowest wave vector allowed (consistent with periodic boundary conditions) to just above the colloidal particle static structure factor peak. Plots of $\ln[F(k,\tau)]$ against $k^2\tau$ which exhibit regions of constant slope imply exponential decays in time, or simple Brownian diffusion. The fits of the form given in Eq. (24) are also shown in Fig. 9 (lines).

For an extremely dilute colloidal suspension, the effects of direct colloidal particle interactions are negligible due to the large average distances between neighboring particles. This means their dynamics are governed by random collisions with the surrounding solvent, so they effectively move as Brownian particles. The $F(k,t)$ in these dilute suspensions ($\Phi \approx 0.01$) decay as a single exponential with a k-independent diffusion coefficient. This is also seen in light scattering experiments [7] (although there is a small k dependence in the diffusion coefficient which is associated with polydispersity) and in our previous work using the current computer simulation model [25].

Calculations for $F(k,t)$ of a system at $\Phi = 0.27$ are shown in Fig. 9(a). The decay for all wave vectors is (almost) linear, just as in a dilute system, but the slope of the decay changes with each new k. This implies the existence of time-independent diffusion with a wave vector dependent diffusion coefficient $D(k)$. With the plot displayed in this way, the lowest-k value has the largest slope, indicating it has the largest effective diffusion coefficient.

As the wave vector is increased, the slope decreases up to the structure factor peak of $(kd)_{\max} = 6.24$ (circles). At wave vectors above the structure factor peak, we see a reversal in the trend, where the slope is seen to have increased at $kd = 7.27$ (triangles) showing a minimum in the diffusion coefficient at

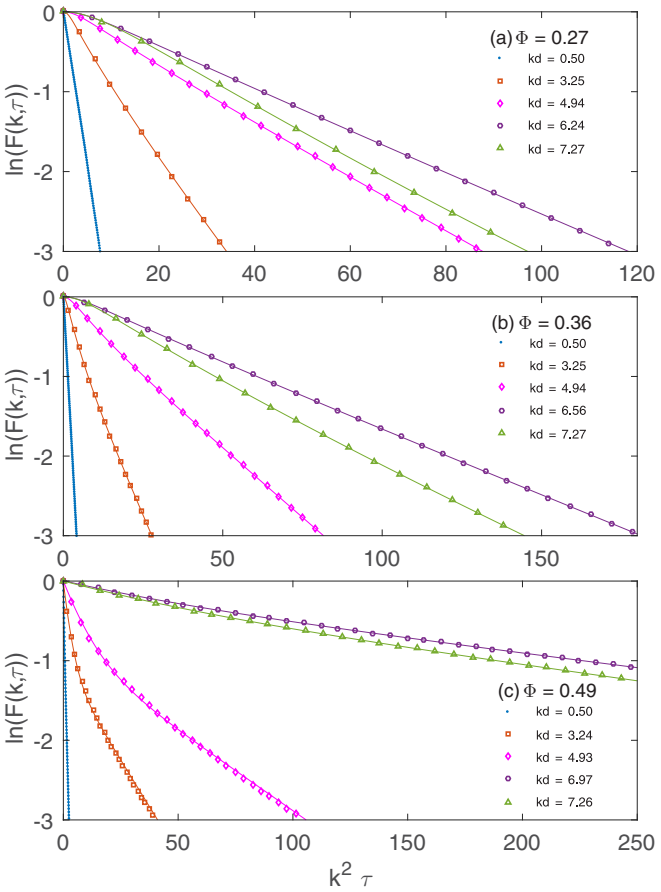

FIG. 9. Plot of the $\ln[F(k,\tau)]$ against $k^2\tau$ for packing fractions of (a) 0.27, (b) 0.36, and (c) 0.49 for the kd values given in the legend. The data for the lowest kd (dots) correspond to the lowest kd possible to calculate based on the box dimensions, and the second largest value (circles) corresponds to the colloidal particle static structure factor peak.

the structure factor peak. It is well verified that in concentrated colloidal suspensions the effective diffusion coefficient has a minimum at the peak in $S(k)$ [7,9]. This minimum reflects the fact that the strong fluctuations that occur at the peak will decay slower than the weak fluctuations away from the peak. It should be noted though that in order to properly fit the data for $\Phi = 0.27$, the second diffusive mode was still needed (although it was very weak).

Figure 9 also reveals the change in behavior of $F(k,t)$ as the packing fraction increases towards the freezing point. At $\Phi = 0.36$ [Fig. 9(b)], the slope is also seen to decrease as the wave vector increases, and has a minimum at the structure factor peak. Interestingly, the spread in the slopes has been greatly increased compared to $\Phi = 0.27$. The slope at the lowest wave vector ($kd = 0.50$) has increased compared to $\Phi = 0.27$ at the same wave vector (note the change in scale on the x axis), while the slope at the structure factor peak ($kd = 6.56$) has decreased. The increasing slope at low wave vectors is the result of the increase in the mutual diffusion coefficient (shown in Fig. 8) as it is this coefficient that governs the decay of $F(k,t)$ in the low wave vector limit. The decay of $\ln[F(k,t)]$ for all wave vectors at $\Phi = 0.36$ is also not quite linear, with

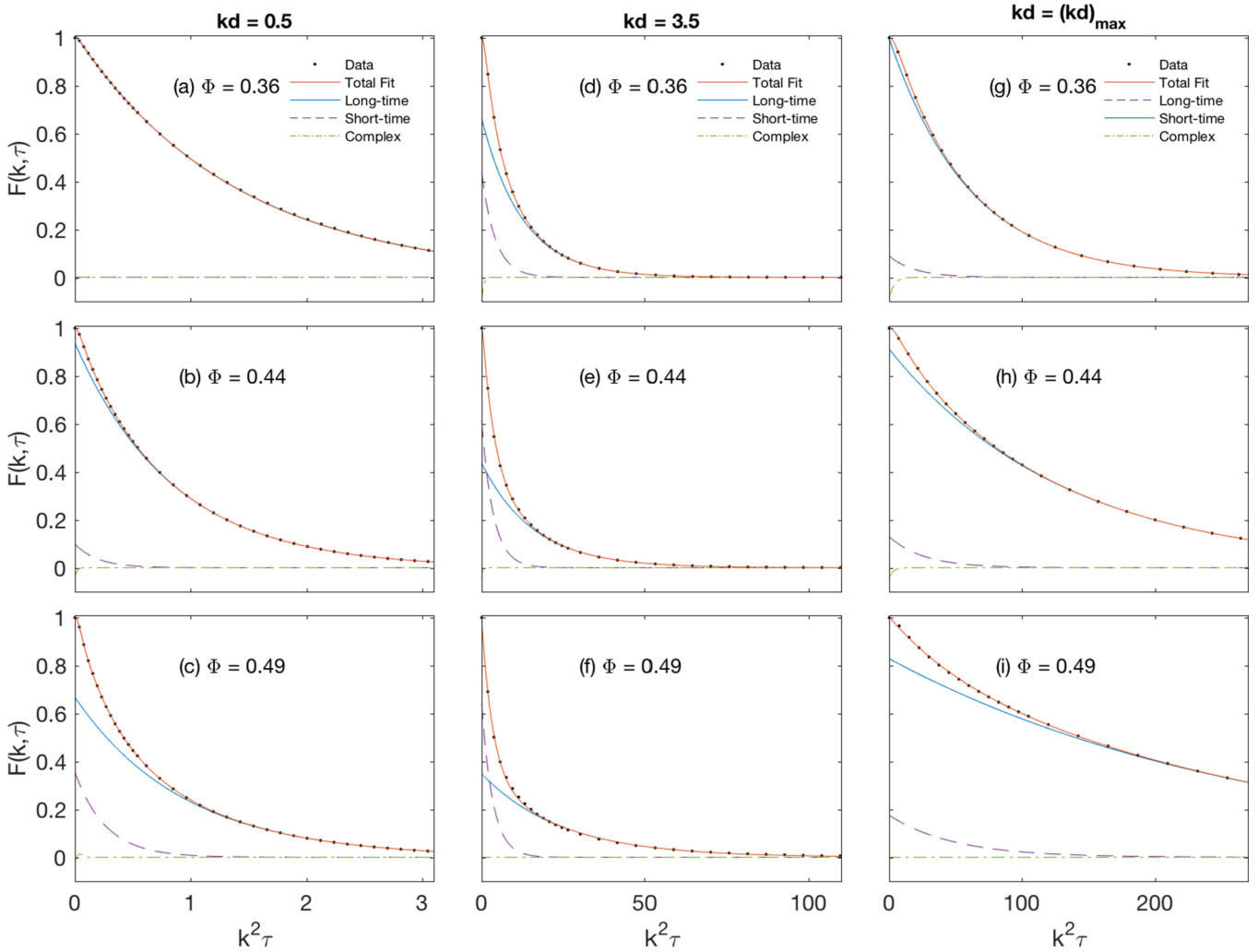

FIG. 10. Plot of $F(k,t)$ data (symbols) for the three indicated packing fractions Φ together with the multiexponential fit described in the text (red solid line through the data points). The left frames [(a)–(c)] are at a low wave vector ($kd = 0.5$), the middle frames [(d)–(f)] are at a wave vector halfway to the structure factor peak ($kd = 3.5$), and the right frames [(g)–(i)] are at the wave vector that corresponds to the structure factor peak ($kd \approx 7$). The various components of the fit function are also displayed separately according to the legend. Short and long time denote the real exponential terms ordered by increasing decay time. Complex denotes the sum of the two complex conjugate exponentials, amounting to a damped oscillatory function. For graphical clarity, not all available data points have been displayed.

a slight nonlinearity of the line of best fit most clearly seen at $kd = 4.94$ (diamonds). This is indicative that the effective diffusion coefficient is becoming time dependent. Just below freezing at $\Phi = 0.49$ [Fig. 9(c)], the two decay modes are clearly seen, with a significant nonlinearity occurring at wave vectors between zero and the structure factor peak.

This method of fitting Eq. (24) to find the behavior of the short-time and long-time diffusion coefficients is similar to that done to experimental results by Orsi *et al.* [27]. The multiexponential analysis procedure that we performed on our data allows the contributions from the individual terms in Eq. (24) to be separated and studied. To better quantify the behavior of the modes and their wave vector and packing fraction dependence, we have plotted the total fit and the individual contributions in Fig. 10. This was done for the three highest Φ values 0.36, 0.44, and 0.49 as all lower Φ exhibit mostly single exponential decay.

The third term in Eq. (24) is the sum of two complex conjugate exponentials, which gives a damped cosine function. This mode is labeled complex in Fig. 10, and is seen to be strongly damped and characterized by a very low amplitude. This mode mainly determines the behavior of $F(k,\tau)$ at very short times where nonexponential decay is observed. We observe nonexponential behavior at short times as the dynamics transitions from atomic to Brownian motion. The size and mass ratio compared to the solvent is 4.03:1 and 50:1, respectively, rather than being effectively infinite as it would be for a real Brownian particle. Therefore, at very short delay times the behavior is not diffusive, though this nondiffusive mode quickly decays to zero leaving the two diffusive modes to dominate.

The two diffusive modes [the two real exponential terms in Eq. (24)] show interesting and complex dependence on packing fraction and wave vector. The left frames [(a)–(c)] of Fig. 10 show the decay at a very low wave vector ($kd = 0.5$). In this low wave vector limit, $F(k,\tau)$ is expected to approach a single exponential as the wavelengths being probed approach the macroscopic diffusive limit (infinite

wavelength). This behavior is observed in the low-k results for the packing fraction of $\Phi = 0.36$ [Fig. 10(a)] where the dominant contribution comes from the long-time diffusive mode, and the short-time mode has an amplitude that is near zero.

For the higher packing fractions in the low-k region [Figs. 10(b) and 10(c)], the long-time mode still dominates, but the short-time mode is nonzero and has a greater contribution. The second mode has a larger contribution because the wave vector being studied is not low enough to be in the macroscopic diffusive limit at these packing fractions. As the freezing point is approached, the maximum wave vector at which macroscopic diffusive behavior was observed decreases. This maximum wave vector may even be unattainable when the fluid crystallizes, as the system would no longer be homogeneous. This may be an important indicator of the onset of crystallization in a system.

The middle frames [(d)–(f)] of Fig. 10 show the decay at $kd = 3.5$ (which is roughly halfway to the peak in the structure factor). A comparison between data at these wave vectors and those at lower wave vectors shows there is a large decrease in the decay rate (note the expanded scale). This indicates that the effective short- and long-time diffusion coefficients have greatly decreased as the wave vector has increased. We also see an increase in the amplitude of the faster decay mode, showing that it has a larger contribution to the total fit.

Just as we observed at low wave vectors, the contribution of the short-time mode again increases as the packing fraction is increased. This can be seen by comparing the amplitude of the short-time mode in Figs. 10(d) and 10(f). At the larger packing fractions of $\phi = 0.44$ and 0.49, the amplitude of the short-time mode is actually larger than the long-time mode [seen in Figs. 10(e) and 10(f)].

The right frames [(g)–(i)] of Fig. 10 show the decay of $F(k,\tau)$ at kd values that correspond to the main peak in the colloidal component structure factor. The effective diffusion coefficients continue to show a monotonic decrease as the packing fraction increases, shown by the increased decay time. As mentioned earlier, this is consistent with experimental results which show a minimum in the diffusion coefficients at the structure factor peak [7,9]. The amplitudes of the modes, however, do not show monotonic dependence on the wave vector. The long-time diffusive mode amplitude has increased in the approach to the structure factor peak, while the short-time one has decreased.

To display in more detail the complete behavior of the amplitudes and their dependence on packing fraction and wave vector, Fig. 11 shows the amplitudes of the two diffusive decay modes at the same packing fractions. As previously observed, at low wave vectors the amplitude of the long-time diffusive mode is almost unity, while the short-time one is almost zero. This indicates that the decay of $F(k,\tau)$ is close to a single exponential (as expected in the macroscopic diffusive limit).

Because the long-time mode still has a nonzero amplitude in the $k \to 0$ limit, it can be identified as a thermodynamic mode, where its decay rate in the macroscopic diffusive limit can be related to a thermodynamic quantity (later we show this to be the mutual diffusion coefficient). The short-time mode only exists for nonzero k, so can be identified as a kinetic mode which can not be related to any bulk property of the fluid. It can

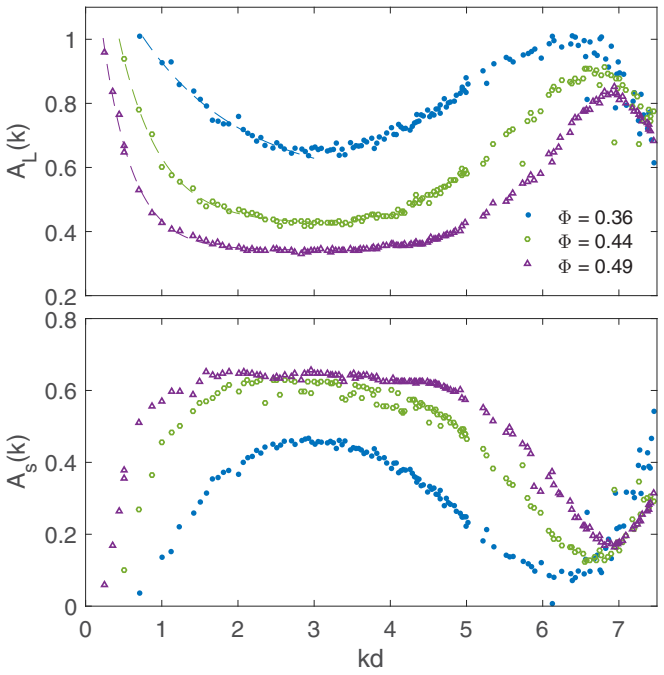

FIG. 11. Plot of the amplitudes of the long-time D_L (top) and short-time D_S (bottom) exponential decay modes for packing fractions of 0.36 (dots), 0.44 (circles), and 0.49 (triangles). Shifted exponential lines of best fit of the low-k data for D_L are also shown (dashed lines).

also be seen that the wave vector where the long-time diffusive mode amplitude goes to unity (or the short-time amplitude goes to zero) decreases as the freezing point is approached, and will most likely disappear when crystallization occurs.

To better quantify the packing fraction where the macroscopic diffusive limit can not be reached, a simple shifted exponential fit was done to the small wave vectors values of A_L as shown in Fig. 11 (dashed lines). The kd values where the exponential fits equal unity (when the macroscopic diffusive limit is reached) are displayed in Fig. 12 and are denoted by $(kd)_M$. These three $(kd)_M$ values are shown to have a linear dependence on Φ, and an extrapolation of the linear fit to the Φ axis identifies the packing fraction of $\Phi \approx 0.546$ as when the diffusive limit disappears. This is extremely close to the melting point of $\Phi = 0.545$ where HS systems completely crystallize and macroscopic diffusion is no longer possible.

The nonzero wave vector behavior of the amplitudes shows complex dependence. As seen in Fig. 11, the short-time mode amplitude decreases to zero as $kd \to 0$, has a local maximum at $kd \approx 3$, and then a local minimum at the structure factor peak. It is interesting to note that although the local minimum at the structure factor peak depends on the packing fraction, the local maximum at $kd \approx 3$ does not. A complete explanation of the interesting nonmonotonic behavior of the mode amplitudes is currently not known.

Unlike the amplitudes, the effective long- and short-time diffusion coefficients show a monotonic dependence on the wave vector between $kd = 0$ and $(kd)_{\max}$. Previous DLS results [28] showed that the inverse of the effective diffusion coefficients correlate well with the static structure factor. To

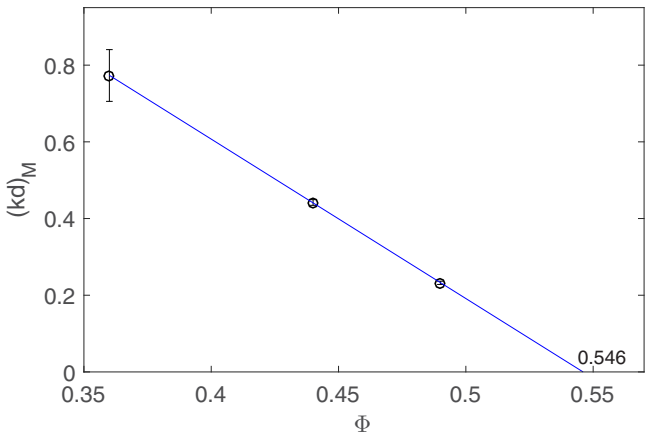

FIG. 12. Plot of the maximum wave vector $(kd)_M$ when single exponential decay of the intermediate scattering function is observed at each packing fraction Φ. Error bars calculated based on the standard errors of fit coefficients in Fig. 11. Unweighted linear fit also shown with x intercept of 0.546.

check that this is also true for this model colloid, the inverse of the short- and long-time diffusion coefficients are plotted in Fig. 13, along with the scaled static structure factors.

In line with what is seen in experimental studies, the inverses of the diffusion coefficients roughly follow the static structure factor. Both have peaks at $(kd)_{\max}$, which corresponds to the value of the structure factor peak. Also, both approach zero in the $k \to 0$ limit. From this we can deduce that the diffusion coefficients (inverse of data in Fig. 13) have maxima at $k \to 0$ and minima at the structure factor peak (as expected).

The similarity of the shapes of D_L and D_s implies that they may be directly proportional, which would confirm the scaling law proposed by Segrè and Pusey [28]. In order to see if this scaling is observed with the current model, Fig. 14 shows the calculated ratio D_s/D_L for all available k vectors at the packing fractions of 0.36, 0.44, and 0.49.

Segrè and Pusey [28] studied the intermediate scattering function of an experimental colloidal suspension over the wave vector range $2 \leqslant kd \leqslant 7.8$ and found the ratio D_s/D_L was constant for $5 \leqslant kd \leqslant 7.8$ (around the structure factor peak). They found that by dividing $\ln[F(k,\tau)]$ by $D_s k^2$, the decays at the wave vectors around the structure factor peak fell onto (roughly) a single master curve. Their work was done for a packing fraction of 0.465.

Data for $\Phi = 0.44$ (which is the closest Φ to that studied by Segrè and Pusey) is shown in Fig. 14. We see that the ratio is not constant, but has a wave vector dependence. Even in the region studied by Segrè and Pusey ($5 \leqslant kd \leqslant 7.8$), the ratio is not constant, showing a local maximum in this region.

The data for all packing fractions in Fig. 14 exhibit the same general shape, but the uncertainties are larger where the second diffusive mode is weak. Each packing fraction shows a slight peak around the position of the structure factor peak.

At $kd < 5$, there is a slight increase in the ratio with a local maximum occurring at $\approx 2.6kd$. This is around the range where

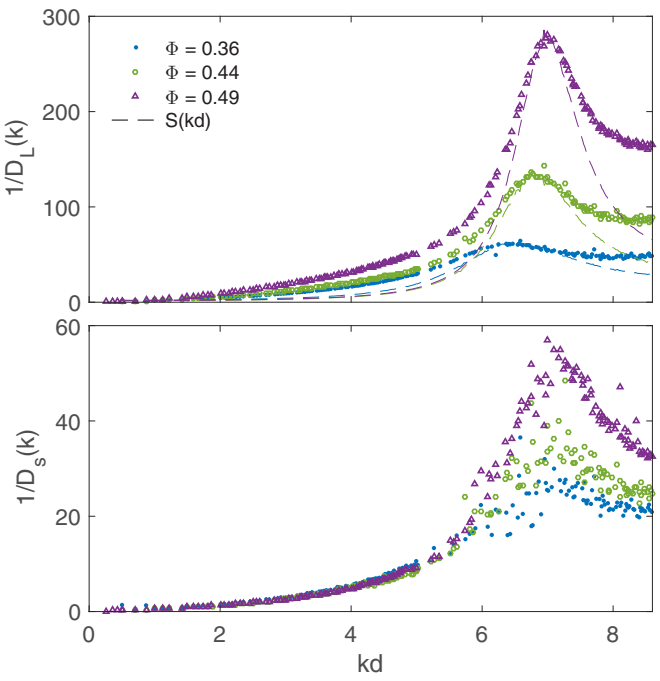

FIG. 13. Inverse diffusion coefficients of the long-time D_L and short-time D_S exponential decay modes for packing fractions of 0.36 (dots), 0.44 (circles), and 0.49 (triangles). Static structure factor data are also plotted (dashed lines) where the data have been scaled to match at the peaks.

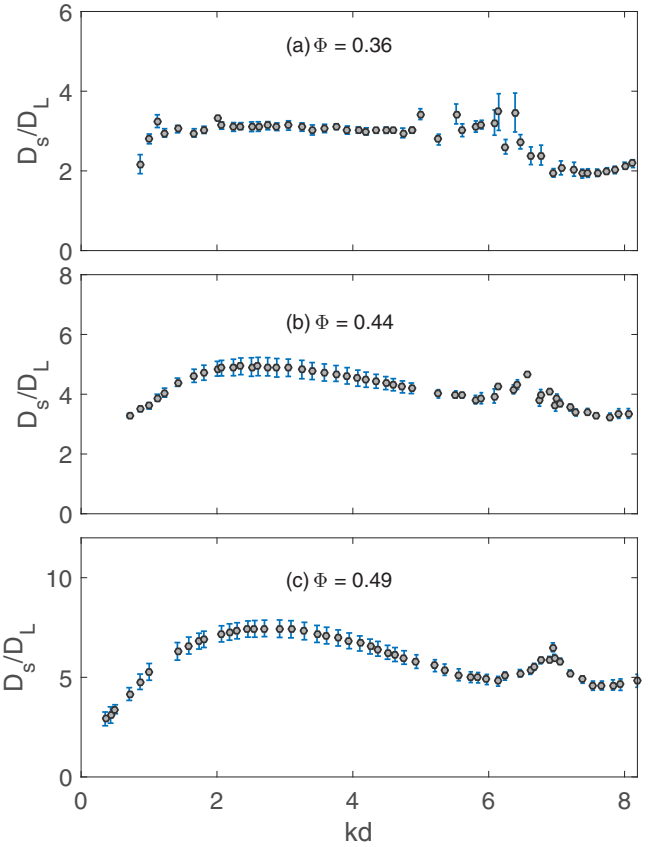

FIG. 14. Plot of the ratio D_s/D_L for packing fractions of (a) 0.36, (b) 0.44, and (c) 0.49.

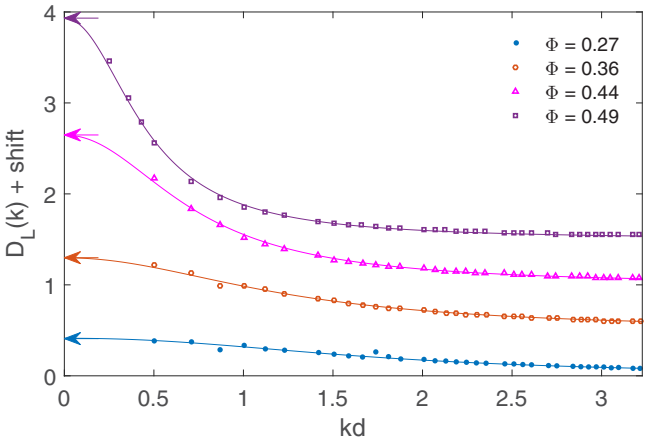

FIG. 15. Plot of low-k values of the long-time diffusion coefficient D_L for packing fractions of 0.27 (dots), 0.36 (circles), 0.44 (triangles), and 0.49 (squares). Arrows on y axis indicate the value of the mutual diffusion coefficients calculated for the corresponding packing fractions. Fits of the form given in Eq. (26) are also shown. Corresponding plots have been shifted up by increments of 0.5 for clarity.

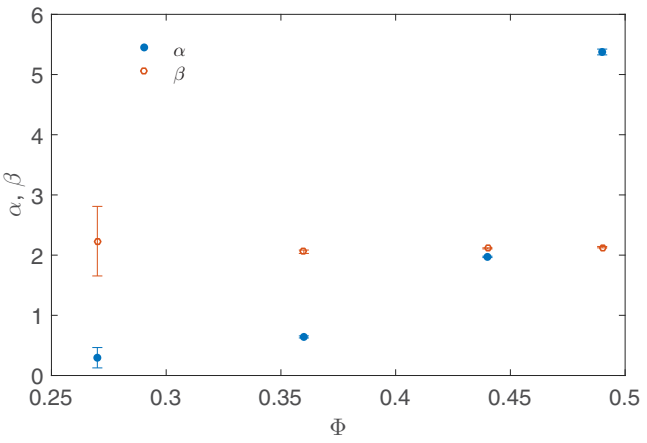

FIG. 16. Packing fraction dependence of fit coefficients α and β from Eq. (26). Error bars calculated based on the standard errors of fit coefficients in Fig. 15.

nonlinearity of $\ln[F(k,\tau)]$ is most noticeable. This is partly due to the increase in the ratio, but also due to the increase in the amplitude of the faster mode in this region. At extremely small wave vectors ($kd < 1.5$), there is a rapid decrease in the ratio. This ratio could possibly extrapolate to 2 at zero wave vector, but this is impossible to determine from the current data. The average ratio over the whole range of wave vectors increases with packing fraction, showing the divergence of the two decay modes as the freezing point is approached.

Since the $k \to 0$ behavior of $F(k,t)$ should be given by the solution to the hydrodynamic equation (13), the decay should be a single exponential with a decay coefficient equal to the mutual diffusion coefficient D_m. To check this, we have plotted the low-k values of D_L in Fig. 15 (symbols) along with the mutual diffusion coefficients calculated from equilibrium MD using the Green-Kubo and Kirkwood-Buff theory (arrows). The data for each Φ given in Fig. 15 have been shifted up by increments of 0.5 for clarity.

Previous work done by Hansen *et al.* [59] showed that the wave vector dependence of the viscosity for a simple fluid could be fitted well with a Lorentzian type function with a variable wave vector exponent. To see if this is also true for the wave vector dependent diffusion coefficient, we have followed the same procedure and fitted the low-k data with a similar functional form given as

$$D_L(k) = \frac{D_m}{1 + \alpha |k|^\beta}, \tag{26}$$

where the coefficients α and β are free fitting parameters that are not wave vector dependent. Figure 15 shows that this functional form fits the data quite well over the range of wave vectors investigated at each packing fraction.

The packing fraction dependence of the parameters α and β are shown in Fig. 16. From this figure it is seen that the exponent β is fairly constant over the range of packing fractions studied. Its value is very close to 2, which indicates that the fitting function is in fact a Lorentzian. The α coefficient, however, shows a strong dependence on the packing fraction. As the packing fraction increases towards the freezing point, α increases by a factor of 18 over the range studied. The increasing value of α reinforces the idea that the wave vector needed to achieve the macroscopic diffusive limit decreases as the packing fraction increases. This arises because as α increases, lower values of k are needed before the term $\alpha|k|^\beta$ in Eq. (26) is effectively zero.

V. CONCLUSION

Molecular dynamics simulations were conducted on a model colloidal suspension with explicit solvent. In this study, we extended previous work and further tested the validity of the model. This was done by studying dynamical properties such as the velocity autocorrelation function, diffusion coefficients, and the intermediate scattering function which were then compared with available experimental data.

The velocity autocorrelation function was found to have velocity reversals for all moderate to high packing fractions ($\Phi \geqslant 0.09$). This behavior is also seen in experimental systems at $\Phi \geqslant 0.289$, but is only observed in single component HS systems at much higher packing fractions ($\Phi \geqslant 0.44$). This indicates that inclusion of a solvent is needed in order to get dynamics which best match experimental colloidal suspensions.

The self-diffusion coefficient was found to decrease as the packing fraction increased, showing that interactions with other colloidal particles inhibit motion through the solvent. This model overpredicted the value of the normalized self-diffusion coefficient, possibly due to the modified interaction parameters used to reduce depletion effects. The self-diffusion coefficient extrapolates to zero near the melting point ($\Phi = 0.544$ compared to $\Phi_m = 0.545$) where the diffusive motion of the colloidal particles is completely inhibited and the system crystallizes.

Unlike the self-diffusion coefficient, the mutual diffusion coefficient was found to increase as the packing fraction increased. This was due almost entirely to the increase in

the thermodynamic factor on the approach to the freezing point. The mutual diffusion coefficient was shown to govern the low-k decay of the intermediate scattering function, and so an increase in the coefficient corresponded to the increase in the decay rate of the intermediate scattering function at low wave vectors.

Lastly, after performing a multiexponential analysis of the intermediate scattering function we found that the decay can be accurately modeled with two real exponentials (for the two diffusive decay modes) and one complex conjugate pair of exponentials (for the short-time nondiffusive behavior). The two real exponential decay modes are similar to what is seen in experimental systems, and are usually associated with long- and short-time diffusion coefficients.

Both the short- and long-time diffusion coefficients decreased monotonically with increasing wave vector, while their corresponding mode amplitudes showed a nonmonotonic dependence. The amplitude of the short-time exponential mode decreased to zero in the $k \to 0$ macroscopic diffusive limit, indicating that this is a kinetic mode which only exists for nonzero k. The long-time mode remained in the low-k limit, leading to a single exponential decay of the intermediate scattering function. The decay rate of this thermodynamic mode in the $k \to 0$ limit was found to be equal to the macroscopic mutual diffusion coefficient calculated independently from Green-Kubo and Kirkwood-Buff theory.

We found that the maximum wave vector for which macroscopic diffusive behaviour could be observed (single exponential decay) decreased as the packing fraction increased, and a simple extrapolation shows the maximum wave vector going to zero at the melting point where macroscopic diffusion can no longer occur. This indicates that the packing fraction where the fluid completely crystallizes may be predicted by studying the decay of the density fluctuations of the fluid well below the melting point.

By studying the two diffusive modes we were also able to test the scaling law proposed by Segrè and Pusey. We found that the ratio of the long- and short-time diffusion coefficients around the structure factor peak was not constant, but had wave vector dependent behavior, in disagreement with the proposed scaling law.

ACKNOWLEDGMENTS

This research was undertaken with the assistance of resources from the National Computational Infrastructure (NCI), which is supported by the Australian Government. S.D.W.H. acknowledges the support of the Australian Government through the Australian Postgraduate Awards (APA) scheme. The authors would like to thank Professor W. van Megen for helpful comments on the manuscript.

[1] U. Gasser, J. Phys.: Condens. Matter. **21**, 203101 (2009).
[2] R. P. Sear, J. Phys.: Condens. Matter. **19**, 033101 (2007).
[3] V. L. Colvin, MRS Bull. **26**, 637 (2001).
[4] H. Imai and Y. Oaki, MRS Bull. **35**, 138 (2010).
[5] V. A. Martinez, J. H. J. Thijssen, F. Zontone, W. van Megen, and G. Bryant, J. Chem. Phys. **134**, 054505 (2011).
[6] P. N. Pusey and W. van Megen, Nature (London) **320**, 340 (1986).
[7] W. van Megen, R. H. Ottewill, S. M. Owens, and P. N. Pusey, J. Chem. Phys. **82**, 508 (1985).
[8] W. van Megen and P. N. Pusey, Phys. Rev. A **43**, 5429 (1991).
[9] P. N. Segrè, O. P. Behrend, and P. N. Pusey, Phys. Rev. E **52**, 5070 (1995).
[10] W. van Megen, T. C. Mortensen, S. R. Williams and, J. Müller, Phys. Rev. E **58**, 6073 (1998).
[11] S. Martin, G. Bryant, and W. van Megen, Phys. Rev. E **67**, 061405 (2003).
[12] B. J. Alder and T. E. Wainwright, Phys. Rev. A **1**, 18 (1970).
[13] S. Ramaswamy, Adv. Phys. **50**, 297 (2001).
[14] D. L. Ermak and J. A. McCammon, J. Chem. Phys. **69**, 1352 (1978).
[15] J. F. Brady and J. F. Morris, J. Fluid Mech. **348**, 103 (1997).
[16] J. Rotne and S. Prager, J. Chem. Phys. **50**, 4831 (1969).
[17] H. Yamakawa, J. Chem. Phys. **53**, 436 (1970).
[18] W. C. Soysa, B. Dünweg, and J. R. Prakash, J. Chem. Phys. **143**, 064906 (2015).
[19] A. J. C. Ladd, J. Fluid Mech. **271**, 285 (1994).
[20] A. J. C. Ladd, J. Fluid Mech. **271**, 311 (1994).
[21] R. D. Groot and P. B. Warren, J. Chem. Phys. **107**, 4423 (1997).
[22] A. Malevanets and R. Kapral, J. Chem. Phys. **110**, 8605 (1999).
[23] A. Malevanets and R. Kapral, J. Chem. Phys. **112**, 7260 (2000).
[24] A. Vrabecz and G. Tóth, Mol. Phys. **104**, 1843 (2006).
[25] S. D. W. Hannam, P. J. Daivis, and G. Bryant, Mol. Sim. **42**, 511 (2016).
[26] P. N. Pusey, J. Phys. A: Math. Gen. **11**, 119 (1978).
[27] D. Orsi, A. Fluerasu, A. Moussaid, F. Zontone, L. Cristofolini, and A. Madsen, Phys. Rev. E **85**, 011402 (2012).
[28] P. N. Segrè and P. N. Pusey, Phys. Rev. Lett. **77**, 771 (1996).
[29] L. B. Lurio, D. Lumma, A. R. Sandy, M. A. Borthwick, P. Falus, S. G. J. Mochrie, J. F. Pelletier, M. Sutton, L. Regan, A. Malik, and G. B. Stephenson, Phys. Rev. Lett. **84**, 785 (2000).
[30] D. Evans and G. Morriss, *Statistical Mechanics of Nonequilibrium Liquids*, 3rd ed. (Academic, London, 1990).
[31] J. P. Hansen and I. R. McDonald, *Theory of Simple Liquids* (Elsevier, Amsterdam, 2006).
[32] S. R. de Groot and P. Mazur, *Non-equilibrium Thermodynamics* (Dover, New York, 1984).
[33] J. G. Kirkwood and F. P. Buff, J. Chem. Phys. **19**, 774 (1951).
[34] Y. Zhou and G. H. Miller, J. Phys. Chem. **100**, 5516 (1996).
[35] N. A. T. Miller, P. J. Daivis, I. K. Snook, and B. D. Todd, J. Chem. Phys. **139**, 144504 (2013).
[36] Note that [35] uses an incorrect relation for the conversion of the thermodynamic factor to mass concentration units and contains some inaccurate results for $G_{\alpha\beta}$. An erratum is currently being prepared.
[37] J. W. Nichols, S. G. Moore, and D. R. Wheeler, Phys. Rev. E. **80**, 051203 (2009).
[38] F. Barocchi, U. Bafile, and M. Sampoli, Phys. Rev. E **85**, 022102 (2012).
[39] F. Barocchi and U. Bafile, Phys. Rev. E **87**, 062133 (2013).

[40] F. Barocchi, E. Guarini, and U. Bafile, Phys. Rev. E **90**, 032106 (2014).
[41] MATLAB version 8.5 (R2015a), (The MathWorks Inc., Natick, MA, 2016).
[42] S. Hess, M. Kröger, and H. Voigt, Phys. A (Amsterdam) **250**, 58 (1998).
[43] M. McPhie, Ph.D. thesis, RMIT University, 2003.
[44] I. Snook, B. O'Malley, M. McPhie, and P. Daivis, J. Mol. Liq. **103-104**, 405 (2003).
[45] S. Plimpton, J. Comput. Phys. **117**, 1 (1995)
[46] M. E. Tuckerman, J. Alejandre, R. López-Rendón, A. L. Jochim, and G. J. Martyna, J. Phys. A: Math. Gen. **39**, 5629 (2006).
[47] S. R. Williams, G. Bryant, I. K. Snook, and W. van Megen, Phys. Rev. Lett. **96**, 087801 (2006).
[48] S. R. Williams, P. McGlynn, G. Bryant, I. K. Snook, and W. van Megen, Phys. Rev. E. **74**, 031204 (2006).
[49] R. Zwanzig and M. Bixon, Phys. Rev. A **2**, 2005 (1970).
[50] W. van Megen, Phys. Rev. E. **73**, 020503 (2006).
[51] I. Moriguchi, J. Chem. Phys. **106**, 8624 (1997).
[52] W. van Megen and S. M. Underwood, J. Chem. Phys. **91**, 552 (1989).
[53] A. van Blaaderen, J. Peetermans, G. Maret, and J. K. G. Dhont, J. Chem. Phys. **96**, 4591 (1992).
[54] A. J. Banchio, G. Nägele, and J. Bergenholtz, J. Chem. Phys. **113**, 3381 (2000).
[55] W. van Megen, Phys. Rev. E. **76**, 061401 (2007).
[56] B. Widom, J. Chem. Phys. **39**, 2808 (1963).
[57] K. Schnell, T. J. H. Vlugt, J. M. Simon, D. Bedeaux, and S. Kjelstrup, Chem. Phys. Lett. **504**, 199 (2011).
[58] J. W. Nichols and D. R. Wheeler, Ind. Eng. Chem. Res. **54**, 12156 (2015).
[59] J. S. Hansen, P. J. Daivis, K. P. Travis, and B. D. Todd, Phys. Rev. E. **76**, 041121 (2007).